Probing the Sun's Near Surface Shear Layer using HMI Spherical Harmonic Coefficients

S. C. Tripathy[1], K. Jain[1], S. Kholikov[1,2] and R. Komm[1]

[1] National Solar Observatory, 3665 Discovery Dr., Boulder, CO 80303, USA
[2] Institute of Fundamental and Applied Research, National Research University, TIIAME, Uzbekistan

Abstract. We have measured zonal and meridional components of subsurface flows up to a depth of 30 Mm below the solar surface by applying the technique of ring diagram on Dopplergrams which are constructed from the spherical harmonic (SH) coefficients. The SH coefficients are obtained from the Helioseismic and Magnetic Imager (HMI) full-disk Dopplergrams. We find a good agreement and some differences between the flows obtained in this study with those from the traditional methods using direct Dopplergrams.

Keywords. Solar physics, Helioseismology, Solar interior, Solar oscillations, Solar activity, Solar convection zone, Solar rotation, Solar meridional circulation

1. Introduction

Helioseismic studies have illustrated that the most significant changes with the solar cycle occur in the near-surface shear layer (NSSL) occupying outer 5% or about 35 Mm of the Sun by radius. Within this relatively thin layer, the density changes by several orders of magnitude and the rotation rate shows a local maxima. It is also believed that a nonlinear $\alpha\Omega$ dynamo could be operating in this layer where the velocity shear converts a part of the poloidal magnetic field into the toroidal field. The existence of this secondary dynamo is in addition to the global dynamo operating in the tachocline region and may be responsible for the small-scale field of the quiet Sun (Brandenburg 2013). However, the dynamics of NSSL is poorly understood mainly because of the complex interactions between rotation, magnetism and convection. The advent of high-resolution Doppler observations from both space-borne and ground-based instruments, in conjunction with local helioseismic techniques such as ring-diagram (Hill 1988) and time-distance (Duvall et al. 1993), have made it possible to infer the subsurface flows in NSSL and their temporal evolution (Zhao & Kosovichev 2004; Basu & Antia 2010; Komm et al. 2018; Lin & Chou 2018). But local helioseismology techniques are limited in the depth range that can be probed. In particular most of the studies using ring-diagram analysis is confined to a depth of 15 Mm. Only a handful of studies have used large-aperture tiles to analyse flows up to a depth of 30 Mm (González Hernández *et al.* 2006; Komm 2021).

In this context, we measure zonal and meridional components of the horizontal flows up to a depth of 30 Mm below the surface during the first six and half years of the Helioseismic and Magnetic Imager (HMI) observations on board Solar Dynamics Observatory (SDO). We use a non-traditional method comprising of spherical harmonic (SH) coefficients derived from the full-disk Dopplergrams and the ring-diagram (RD) technique. This method has the advantage to infer flows from low-resolution as well as high-resolution Dopplergrams.

2. Data and Analysis Technique

We use HMI SH coefficient time series† for $\ell = 0$ to 400 obtained from the Joint Science Operation Center (JSOC) covering the period 2010 May 1 to 2016 December 31. Each time series is organized as series of individual (n, ℓ, m) coefficients and are 72 days long. We also
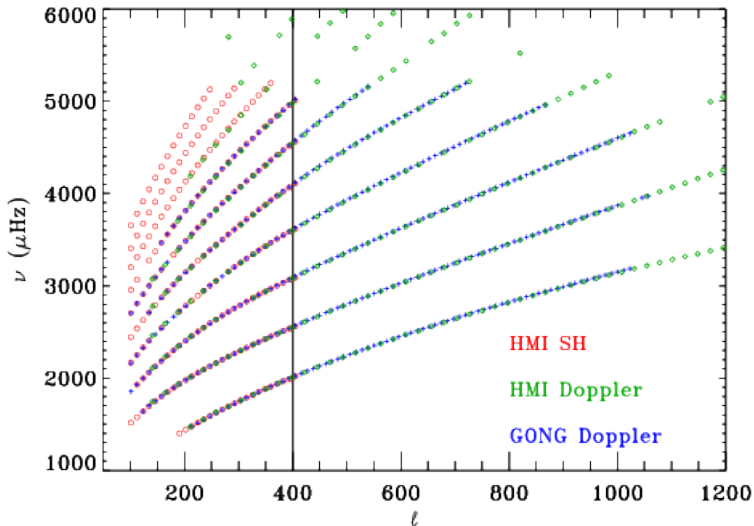
† series name: hmi.ap_V_sht_gf_72d

Figure 1. A typical ℓ-ν diagram showing the distribution of the fitted modes at the disk center using HMI spherical harmonic coefficients (red circles), HMI Dopplergrams (green diamonds) and the GONG Dopplergrams (blue plus). Vertical line at $\ell = 400$ defines the boundary of the fitted modes using spherical harmonic coefficients.

download the window function of each series to track the duty cycle. Use of this SH time series has several advantages as these have been generated from the velocity images which are corrected for known systematics, e.g., image scale, cubic distortion, CCD misalignment, inclination error and CCD tilt *etc*. The Dopplergrams were further detrended and gap filled. A description of all the corrections applied to the time series along with other details are provided in Larson & Schou (2018).

Reconstruction of Dopplergrams using the SH coefficient time series (inverse SH decomposition) is carried out following the procedure described in Kholikov et al. (2014)

$$V(\theta, \phi) = \sum_{\ell=0}^{\ell=400} \sum_{m=0}^{\ell} C_l^m P_l^m(\theta) e^{im\phi + \delta\phi} , \qquad (1)$$

where C_l^m are SH coefficients, P_ℓ^m is the associated Legendre polynomial of spherical degree ℓ and order m, θ and ϕ are latitude and longitude, respectively. We also use the differential rotation profile ($\delta\phi$) of Libbrecht and Morrow (1991) to remove the surface differential rotation where tracking is carried out by introducing the surface differential rotation profile into the argument of the complex exponential in the right hand side of Eq. (1). The reconstructed images were then remapped to 187 patches of the size $30° \times 30°$ from disk center to $\pm 60°$ in latitude and $\pm 37.5°$ in longitude spaced by $7.5°$. All the patches were tracked for 1664 min (the time series are divided in to 1664 min time interval to produce the data cubes). A three-dimensional fast Fourier transform (FFT) is applied to each cube in both spatial and temporal directions to obtain a three-dimensional power spectrum which was subsequently processed through the RD pipeline (Corbard et al. 2003). The fitting algorithm in the RD pipeline uses the maximum-likelihood procedure described in Anderson, Duvall, and Jefferies (1990) and fits about 270 modes for n-values between $0 - 9$ and ℓ values between $110 - 400$ in the frequency range of $1400 - 5200$ μHz. Figure 1 displays a typical ℓ-ν diagram comparing modes fitted at the disk center patch for three different data sets. It is evident that we recover most of the input modes in the ℓ range of approximately 100 to 400 (the RD technique does not fit
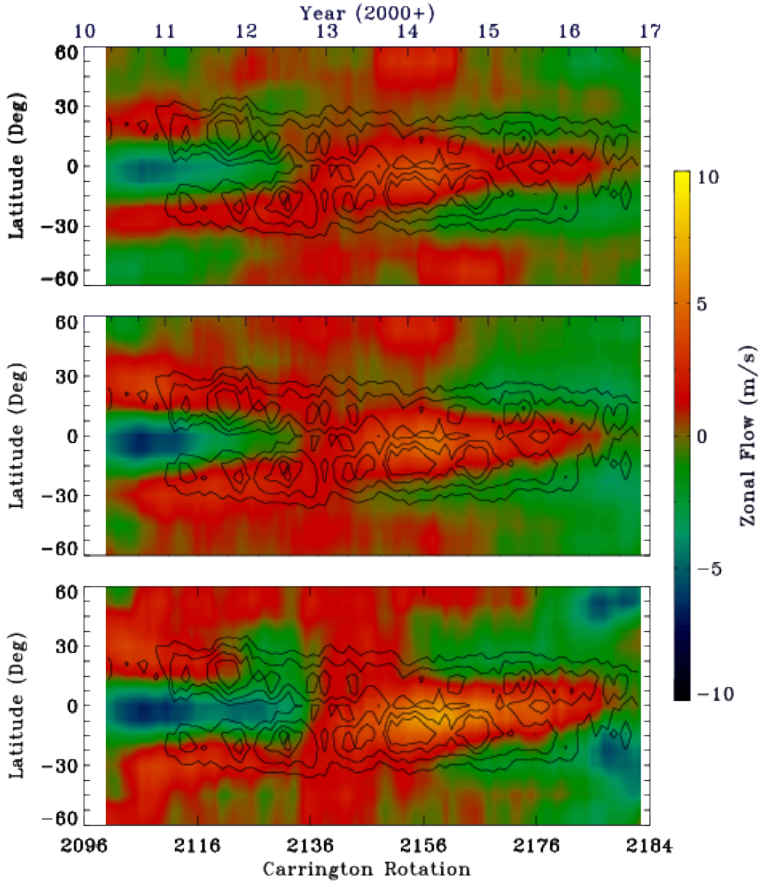
Figure 2. Temporal variation in zonal flow at three different depths: 5.2 ± 2.2 Mm (top), 15 ± 7.2 Mm (middle) and 25.6 ± 7.2 Mm (bottom). The temporal mean has been subtracted at every latitude and depth. Black contours in each panel indicate the magnetic activity.

modes below approximately ℓ of 100). We also note that we fit many more modes in the low ℓ and higher frequency ranges compared to methods using direct Dopplergrams.

The subsurface zonal and meridional flows are finally derived using the Regularized Least Square (RLS) inversion method (Haber et al. 2002). The depth dependence in the inverted flows is known to have significant influence from the mode kernels used in the inversion. The kernels peak sharply near the surface owing to the availability of significant number of modes but are less localized with increasing depth. Thus the depth resolution turns out to be poor resulting in relatively larger errors in deeper layers (Jain et al. 2017). However, in this study we have a limited set of high-degree modes and thus we find that the errors associated with the flows measured closer to the surface are larger compared to deeper depths. We also correct the flows for the annual variation with the solar inclination angle towards Earth (B_0 angle) and other systematic effects following the procedure described in Komm et al. (2015).

3. Results

Figure 2 shows the zonal flow at three depths (5.2 ± 2.2 Mm, 15 ± 7.2 Mm, and 25.6 ± 7.2 Mm) as a function of time and latitude where the mean is subtracted at each latitude and depth. The contours on top of the flows are plotted to depict the evolution of magnetic

activity. The figure illustrates the bands of slower and faster rotation relative to the mean flow, known as torsional oscillations, of few m/s at all depths. These are comparable with those obtained in the traditional methods (e.g., Komm et al. 2018; Zhao et al. 2014, for ring-diagram and time-distance analyses, respectively). As is well known, we find that the bands of faster rotation at mid latitudes are well aligned with the migration of magnetic activity towards the equator but appears about a year earlier before the activity appears at the surface. Although the signature of the poleward branch is visible starting around 2012 during the ascending phase of the cycle, we do not clearly see the branch probably due to the weak cycle 24. Similar results are reported in torsional oscillations derived from the global modes (Howe et al. 2018). Also, the connection between the mid-latitude branch in this solar cycle with the polar branch of the previous cycle is not apparent in the figure due to the temporal coverage. Nevertheless, a close comparison of the zonal flows obtained in Komm et al. (2018) displays similarities as well as some differences in finer details. These differences probably arise due to the different patch sizes used in these studies covering different areas at each grid point and the different smoothing parameters. However the overall patterns are similar in both the studies. Further, we find a discontinuity in the mid-latitude branch in the Northern hemisphere around 2012 in the top and bottom panels of Figure 2 corresponding to 5 and 25 Mm (the band is barely visible in 5 Mm). While the traditional methods provide continuous branches in both hemispheres, our analysis shows the continuous branch to be present in the stronger hemisphere only. It is not clear if this effect is due to smaller temporal coverage which provides different mean values over the two hemispheres. It is also plausible that the corrections that is applied at deeper depths to remove the systematic variations are not optimized.

It is well recognized that the meridional flow is poleward on the surface and in shallow depths and increases gradually with depth. We also find similar results with a peak amplitude of about 15 m/s near the surface and 30 m/s at a depth of 29 Mm. Figure 3 displays the temporal evolution of the meridional flow relative to the mean flow at each latitude and depth for the same depths as the zonal flows. We obtain bands of faster and slower meridional circulation residuals with time but with opposite signs in both hemispheres implying poleward flows as positive values indicate flows to the north and negative values for the flows to the south. At the shallow depths, the band of poleward meridional flow appears at about $60°$ latitude around the mid-2010 (beginning of our data) and slowly migrates towards the equator reaching there in about 2013. A similar result is reported in Komm et al. (2018). But at deeper depths, the flow pattern is reversed; the fast band has changed to the slow band and vice versa and differs from the result of Komm (2021) where results from HMI $30°$ tiles were used. However, we should note that the HMI RD result has a coarser resolution in latitude and longitude since the flow measurement are available only at a grid spacing of $15°$.

The amplitude and direction of the meridional flow at the equator is an important topic in the context of cross-equatorial cancellation of magnetic flux and formation of polar flux. Early investigations that found flows crossing the equator believed it to be an error in the alignment of the telescope since its magnitude is one order smaller than the maximum amplitude of the meridional flow. But recent advances in the surface flux transport models indicate that it plays a crucial role in transporting magnetic flux across the equator from the dominant hemisphere to the other one and thus cancels the excess flux. We further investigate, as shown in Figure 4, the meridional flows at the equator at a depth closer to the surface (averaged over $0.9 – 3.4$ Mm). It is evident that the meridional flows at the equator are small but non-zero. It is mainly positive at the beginning of cycle and oscillates between positive and negative values as the solar cycle progresses which is believed to be a consequence of the imbalance of activity between the two hemispheres. To quantify this flux imbalance, we subtract the magnetic activity index (MAI) of $7.5°$ S tiles from $7.5°$ N tiles. The MAI values for each tile is calculated by tracking and re-mapping line-of-sight magnetograms in the same fashion as Dopplergrams for the same length of time. The absolute values of all pixels higher than a defined threshold are then averaged
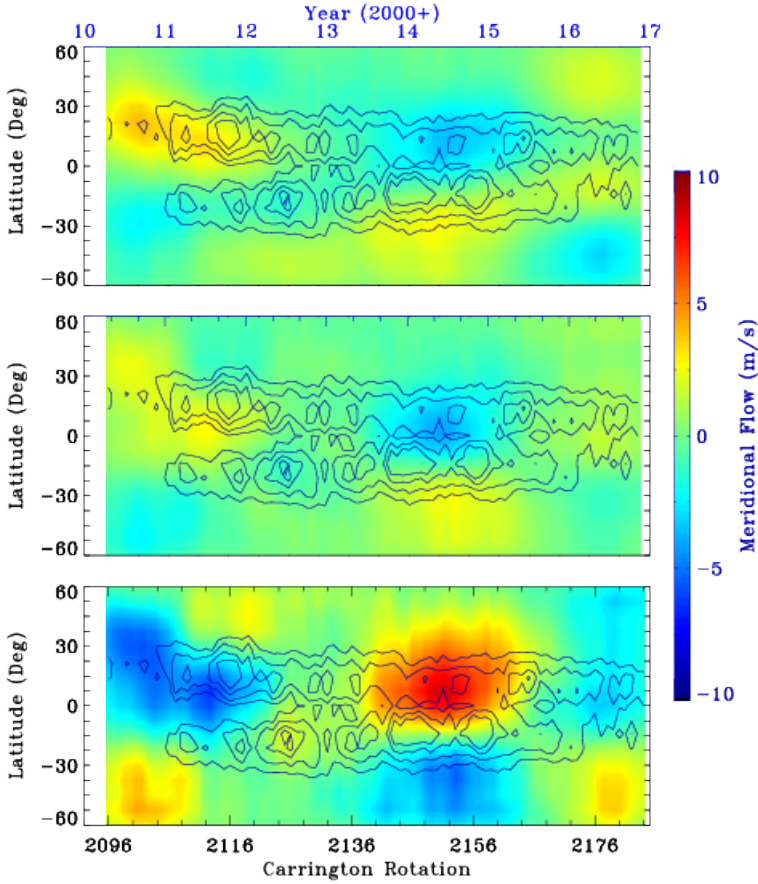
Figure 3. Same as Figure 2 but for meridional flows

to compute the unsigned proxy for magnetic field (MAI). It is evident from Figure 4 that the cross equatorial flows follow the hemisphere with dominant activity. The Pearson's linear cross correlation is found to be 75% confirming the relation between the cross-equatorial flow and strength of the magnetic activity. These findings are in agreement with those reported in Komm (2022) where subsurface flow measurements were derived from $15°$ tiles.

4. Summary

Reconstructing Dopplergrams from the HMI SH coefficients and subsequently applying the ring-diagram technique, we have derived subsurface flows up to a depth of 30 Mm from mid-2010 to the end of 2016. Our preliminary results of zonal and meridional flow profiles mostly agree near the surface and intermediate depth ranges with other studies using observed Dopplergrams. However, the measured meridional flows at greater depths show a flow pattern which is reversed compared to the flows observed near the surface. Although there are limited helioseismic studies which probes the flows at depths greater than 15 Mm using RD technique, our result appears to differ from these findings. It is plausible that the applied empirical correction for the systematic variations has not removed all artifacts. We plan to revisit the correction scheme when flow measurements for whole cycle 24 is computed.
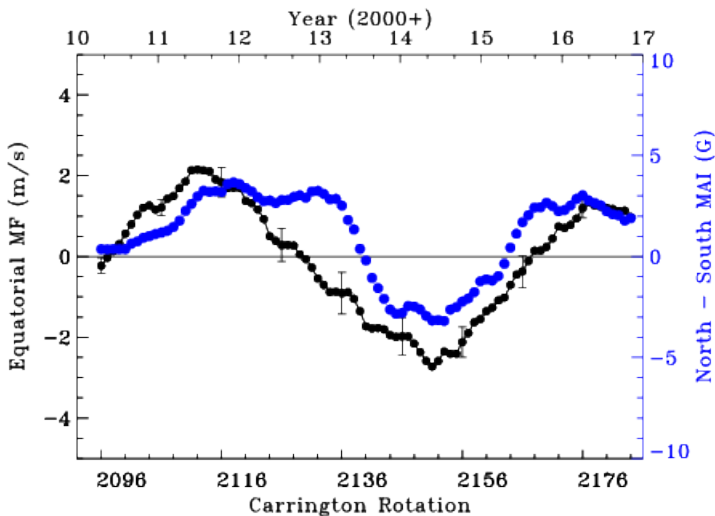
Figure 4. The equatorial meridional flow averaged over the depth range of 0.9 – 3.4 Mm. Positive values indicate northward flows, while negative values indicate southward flows. The blue line represents the strength of the magnetic activity where the MAI of 7.5° S tile is subtracted from the 7.5° N tile. For clarity, the error bars for flow measurements are shown only for few points.

References

Anderson, E.R., Duvall, T.L., and Jefferies, S.M.: 1990, *ApJ*, 364, 699
Basu, S., & Antia, H. M. 2010, *ApJ*, 717, 488
Brandenburg, A.: 2013, *Solar and Astrophysical Dynamos and Magnetic Activity* 294, 387
Corbard, T., Toner, C., Hill, F., et al. 2003, in ESA Special Publication, Vol. 517, GONG+ 2002. Local and
        Global Helioseismology: the Present and Future, ed. H. Sawaya-Lacoste, 255
Duvall, T. L., J., Jefferies, S. M., Harvey, J. W., & Pomerantz, M. A. 1993, *Nature*, 362, 430
González Hernández, I., Komm, R., Hill, F., Howe, R., Corbard, T., and Haber, D.A.: 2006, *ApJ* 638, 576
Haber, D. A., Hindman, B. W., Toomre, J., et al. 2002, *ApJ*, 570, 855
Hill, F. 1988, *ApJ*, 333, 996
Howe, R., Hill, F., Komm, R., Chaplin, W. J., Elsworth, Y., Davies, G. R., and, ...: 2018, *ApJ*, 862, L5
Jain, K., Tripathy, S. C., & Hill, F. 2017, *ApJ*, 849, 94
Kholikov, S., Serebryanskiy, A., & Jackiewicz, J. 2014, *ApJ*, 784, 145
Komm, R.: 2021, *Solar Physics* 296, 174
Komm, R.: 2022, *Solar Physics*, 297, 99
Komm, R., Howe, R., González Hernández, I., & Hill, F. 2015, *Solar Physics*, 290, 1081
Komm, R., Howe, R., & Hill, F. 2018, *Solar Physics*, 293, 145
Larson, T. P., & Schou, J. 2018, *Solar Physics*, 293, 29
Libbrecht, K.G. and Morrow, C.A.: 1991, *Solar Interior and Atmosphere*, 479
Lin, C.-H., & Chou, D.-Y. 2018, *ApJ*, 860, 48
Zhao, J., & Kosovichev, A. G. 2004, *ApJ*, 603, 776
Zhao, J., & Kosovichev, A. G. 2014, *ApJ*, 789, L7